Amplitude-variable output characteristics of triboelectric-electret nanogenerators during multiple working cycles

Hanlu Zhang, Shan Feng, Delong He, Philippe Molinié, Jinbo Bai

Amplitude-variable output characteristics of triboelectric-electret nanogenerators during multiple working cycles

Hanlu Zhang[1], Shan Feng[1], Delong He[1*], Philippe Molinié[2], Jinbo Bai[1*]

[1]Laboratoire Mécanique des Sols, Structures et Matériaux (MSSMat), CNRS UMR 8579, CentraleSupélec, Université Paris-Saclay, 8-10 rue Joliot-Curie, 91190 Gif-sur-Yvette, France

[2]GEEPS Laboratory, CentraleSupélec, 91192 Gif-sur-Yvette Cedex, France

*Corresponding authors: Jinbo Bai (Email: jinbo.bai@ecp.fr); Delong He (Email: delong.he@centralesupelec.fr)

Abstract

Triboelectric-electret nanogenerator (TENG) has recently become a research hotspot in the field of energy harvesting due to its advantages in low-cost, compact structure, broad applicability, and high efficiency. In this work, we calculated the charge transfer process and the output voltage/current/power of a contact-separation mode TENG driven by continuous periodic reciprocating movements with acceleration/deceleration processes, using symbolic computations in MATLAB. The calculated amplitudes of output voltage/current peaks of the TENG vary during multiple working cycles over time in an exponential form and gradually convergence to steady ranges. For the first time, these variations, along with the asymmetry between the output positive and negative voltage/current peaks of the TENG, were attributed to the lag of the charge transfer cycle relative to the periodic movement cycle with both theoretical and experimental evidence. A detailed investigation was conducted on the influence of the initial condition and the load resistance on the variation of TENG output voltage peaks. The optimum load resistance (R_{opt}) was obtained by calculating the average output power of the TENG per movement cycle

(*AvgP*). Both R_{opt} and *AvgP* can be quite different in the steady output ranges from those in the first working cycle if the TENG starts working from the contact state. These results may be important for evaluating and optimizing the output of TENGs in a steady continuous working mode, and for designing TENGs in accordance with their working environment and circuit loads.

Keywords:

triboelectric-electret nanogenerator; continuous working cycles; amplitude-variable output; average output power; initial condition; load resistance.

1. Introduction

Triboelectric-electret nanogenerators (TENGs) are intensively researched in recent years for their broad prospects in efficiently generating electricity from ambient mechanical movements to power diverse electronic devices and construct self-powered systems [1-14], or work as active sensors [15-20]. In comparison with electromagnetic generators, TENGs are light-weight, low-cost, and more efficient in harvesting low-frequent small-scale kinetic energy with simple compact structures [21-28]. Among the five different modes of TENGs, the contact-separation mode has the second largest maximum structural figure-of-merit [29]. Theoretical models for TENGs were well established [30-41]. However, variations in the amplitude of output voltage/current/power of TENGs during multiple continuous working cycles were seldom studied. Besides, some theoretical researches consider only a single separation process of contact-separation mode TENGs and use the instantaneous peak power to obtain the optimum load resistance [31, 33], which may be not appropriate to evaluate the actual performance of TENGs during continuous working. In addition, in previous theoretical calculations/simulations, only movements at constant velocity without acceleration/deceleration processes and movements described by sine or cosine functions were considered [31, 33, 38, 39]. Though some researchers

have found the amplitude-variable output voltage [38] or current [39] of TENGs driven by continuous sine or cosine movements, detailed characteristics and causes of these phenomena need to be further discussed.

In this article, firstly, we gave analytical solutions of the charge transfer differential equation of TENGs with a resistive load and arbitrary initial conditions. Secondly, we defined a piecewise periodic reciprocating movement and used symbolic computations in MATLAB to calculate the charge transfer process and the output voltage/current/power of a specific contact-separation mode TENG driven by the defined movement, with two typical initial conditions. According to obtained results, there are variations in the amplitude of output current/voltage/power peaks of the TENG during multiple movement cycles. The causes of these variations were analyzed according to the calculated charge transfer process. Characteristics of the variation in the amplitude of output voltage peaks of the TENG with different load resistances and initial conditions were discussed in detail. Thirdly, QV cycle diagrams calculated from the two initial conditions were compared, and the optimum load resistance was gotten by calculating the average output power of the TENG per movement cycle. At last, variations in the amplitude of the output voltage peaks of a real TENG driven by a linear motor were verified by both experimental and calculated data. The methods and results presented in this work can be very helpful in evaluating the real performance of TENGs in a certain working environment, which is important for applying TENGs in practical energy harvesting and self-powered systems.

2. Methods

2.1. Model and calculations

A simplified physical model based on the conservation law of charge, Gauss' law, Kirchhoff's law, and Ohm's law for TENGs was used to describe the time-dependent charge

transfer process in TENGs with purely resistive loads [31]. Symbolic computation in MATLAB was used to solve the fundamental differential equation of this model.

2.2. Experimental measurements

A piece of 4 cm × 4 cm sized 100 µm-thick polytetrafluoroethylene (PTFE) film was used as the triboelectric-electret film in the TENG, with conductive copper adhesive tape pasted on one side as the back electrode. The PTFE film was attached on the slider block of a linear motor system (Afag Electro slider ES20-100 with LinMot servo drive and controlled through the LinMot-Talk software), with the naked side outward. A same 4 cm × 4 cm sized aluminum foil was attached to a fixed plate faced with the PTFE film, working as the top electrode for the TENG. The top and back electrodes were connected to an oscilloscope (Wavejet 354A, Lecroy) through high impedance probes to measure the output voltage of the TENG during the back-and-forth movement of the PTFE film driven by the linear motor. The photograph of the TENG and the testing set-up are presented in Fig. S1 in the supporting information. The transferred charge amount was recorded with a Keithley 6514 electrometer. Before each measurement, the top and back electrodes were short-circuited to ensure the electrostatic equilibrium.

3. Modeling

Fig. 1(a) depicts the simplified cross-section structure of the contact-separation mode TENG. In the sketch, $-\sigma$ represents the effective surface charge density on the top side of the electret film, S is the area of the film, ε_0 is the absolute permittivity of air (usually the value of vacuum permittivity is used), ε_r and d_f is the relative permittivity and the thickness of the electret film respectively, $z(t)$ is the time-dependent air gap distance, $Q(t)$ is the time-dependent charge amount on the back electrode, and R is the load resistance in the external circuit. Using the conservation law of charge, the charge amount on the top electrode is given as $\sigma S - Q(t)$. In this

simplified configuration, σ was considered invariable with time, meaning that the electret film was regarded as a perfect electret. Fig. 1(b) shows the equivalent circuit diagram of the TENG. C_{gap} (t) represents the capacitance formed by the air gap between the top electrode and the top side of the electret film, and C_f represents the capacitance formed by the electret film. These two capacitors have one common plate (i.e. the top side of the electret film), and their other two plates (the top and back electrodes) are connected through the resistance load. Therefore, in an electric equilibrium state, the two electrodes should hold an equal electric potential referring to the top side of the electret film.

In the electric equilibrium state, we used $Q_{eq}(t)$ instead of $Q(t)$ to represent the charge amount on the back electrode for distinction. According to the Gauss' law, the back electrode holds an electric potential of $Q_{eq}(t)/C_f$, while the top electrode holds an electric potential of $(\sigma S - Q_{eq}(t))/C_{gap}$ (t), both taking the top side of the electret film as the reference. So, there are

$$\frac{Q_{eq}(t)}{C_f} = \frac{\sigma S - Q_{eq}(t)}{C_{gap}(t)} \tag{1}$$

$$Q_{eq}(t) = \frac{\sigma S C_f}{C_f + C_{gap}(t)} = \frac{\sigma S \varepsilon_r/d_f}{\varepsilon_r/d_f + 1/z(t)} = \frac{\sigma S z(t)}{d_0 + z(t)} \tag{2}$$

, where d_0 is the effective thickness constant of the electret film defined as d_f/ε_r to simply the equation [31]. Q_{eq} is the same as the short-circuit transferred charge in other articles [30, 31], which is reasonable since the two electrodes will always have the same electric potential if they were short-circuited.

With the relative approaching and separating movement between the top electrode and the electret film, C_{gap} changes with z while C_f keeps unchanged, leading to the charge transfer between the top and back electrodes to eliminate the difference in the electric potential caused by

the variation of C_{gap}. According to the Gauss' law, the Kirchhoff's law, and the Ohm's law, the following equation can describe this charge transfer process [31]:

$$R \frac{dQ(t)}{dt} + \frac{Q(t)\,(d_0 + z(t))}{S\,\varepsilon_0} = \frac{\sigma\,z(t)}{\varepsilon_0} \tag{3}$$

. This equation can be analytically solved if a specified initial condition is given and regarding $z(t)$ as a known analytical function. Here, two typical initial conditions are considered. At first, the most used initial condition is used, i.e. $z(0) = 0$ and the two electrodes are in the electric equilibrium state at $t = 0$. According to equation (2), there is

$$Q(0) = Q_{eq}(0) = \frac{\sigma S z(0)}{d_0 + z(0)} = 0 \tag{4}$$

. With this condition, the equation (3) can be solved as

$$Q(t) = e^{-\frac{\int_0^t (d_0 + z(u))\,du}{R\,S\,\varepsilon_0}} \int_0^t \frac{\sigma\,e^{\frac{\int_0^w (d_0 + z(u))\,du}{R\,S\,\varepsilon_0}}\,z(w)}{R\,\varepsilon_0}\,dw \tag{5}$$

, where u and w are intermediate variables for the integration. The output current of the TENG can be derived as

$$I(t) = \frac{dQ(t)}{dt} = \frac{\sigma\,z(t)}{R\,\varepsilon_0} - \frac{e^{-\frac{\int_0^t (d_0 + z(u))\,du}{R\,S\,\varepsilon_0}}(d_0 + z(t))\int_0^t \frac{\sigma\,e^{\frac{\int_0^w (d_0 + z(u))\,du}{R\,S\,\varepsilon_0}}\,z(w)}{R\,\varepsilon_0}\,dw}{R\,S\,\varepsilon_0} \tag{6}$$

. Then the output voltage and power of the TENG can be obtained from the equation (6) and the Ohm's law.

In another case, considering that the top electrode starts to approach the electret film from a distance of z_{max} at $t = 0$ ($z(0) = z_{max}$) and the two electrodes are in the electric equilibrium state at $t = 0$, according to the equation (2), there is

$$Q(0) = Q_{eq}(0) = \frac{\sigma S z_{max}}{d_0 + z_{max}} = Q_{max} \tag{7}$$

, where Q_{max} represents $Q(0)$ under this initial condition. Then $Q(t)$ and $I(t)$ can be solved from the equation (3) as:

$$Q(t) = e^{-\frac{\int_0^t (d_0+z(u))\,du}{R\,S\,\varepsilon_0}} \left[Q_{max} + \int_0^t \frac{\sigma\, e^{\frac{\int_0^w (d_0+z(u))\,du}{R\,S\,\varepsilon_0}} z(w)}{R\,\varepsilon_0}\, dw \right] \tag{8}$$

$$I(t) = \frac{\sigma\, z(t)}{R\,\varepsilon_0} - \frac{e^{\frac{\int_0^t (d_0+z(u))\,du}{R\,S\,\varepsilon_0}}(d_0+z(t))}{R\,S\,\varepsilon_0} \left[Q_{max} + \int_0^t \frac{\sigma\, e^{\frac{\int_0^w (d_0+z(u))\,du}{R\,S\,\varepsilon_0}} z(w)}{R\,\varepsilon_0}\, dw \right] \tag{9}$$

Combining equations (4) ~ (9), the $Q(t)$ and $I(t)$ solved from the equation (3) with an arbitrary initial condition can be given as

$$Q(t) = e^{-\frac{\int_0^t (d_0+z(u))\,du}{R\,S\,\varepsilon_0}} \left[Q(0) + \int_0^t \frac{\sigma\, e^{\frac{\int_0^w (d_0+z(u))\,du}{R\,S\,\varepsilon_0}} z(w)}{R\,\varepsilon_0}\, dw \right] \tag{10}$$

$$I(t) = \frac{\sigma\, z(t)}{R\,\varepsilon_0} - \frac{e^{\frac{\int_0^t (d_0+z(u))\,du}{R\,S\,\varepsilon_0}}(d_0+z(t))}{R\,S\,\varepsilon_0} \left[Q(0) + \int_0^t \frac{\sigma\, e^{\frac{\int_0^w (d_0+z(u))\,du}{R\,S\,\varepsilon_0}} z(w)}{R\,\varepsilon_0}\, dw \right] \tag{11}$$

4. Calculation results

4.1. Parameters for calculations

Based on the modeling part, the output current of a specific TENG can be calculated with given values of parameters. The relative movement between the top electrode and the electret film, described by $z(t)$, is significant to the output of TENGs. In previous researches, mainly two types of movement were studied for the contact-separation mode TENGs. One is a single separation process with a given average velocity, the other one is a simple harmonic movement described by a sine or cosine function. Here, we use a piecewise acceleration-uniform motion-deceleration cyclic movement, which is also an important form of continuous movement, to calculate the output of TENG. For the purpose of comparison, in this section, we used the same

geometrical (thickness and area of electret film), material parameters (permittivity and surface charge density), and movement speed during the uniform motion with the reference [31]. However, we added a large acceleration and deceleration of ±100 m/s² and made the movement reciprocating and cyclic. Detailed parameters' values are given in Table 1. The polarity of charges on the electret film was set as negative since the film used in this work is made with skived PTFE which is one of the most triboelectrically negative materials in the triboelectric series [2]. Though we didn't particularly charge the PTFE film before measurements, it could obtain electrostatic negative charges by the triboelectrification with the top electrode (aluminum foil) during the contact and separation processes. Our experimental results also confirm the negative polarity of these electrostatic charges on the PTFE film.

Table 1 Values of parameters in calculating the output of TENG for comparisons

Parameter	Value
S	58.0644 cm²
ε_r	3.4
d_f	125 μm
σ	10 μC/m²
Maximum gap z_{max}	1 mm
Maximum speed v_1	0.1 m/s
Maximum speed v_2	-0.1 m/s
Acceleration a_1	100 m/s²
Deceleration a_2	-100 m/s²
Deceleration a_3	-100 m/s²
Acceleration a_4	100 m/s²

At first, the case $z(0) = 0$ and $Q(0) = 0$ was considered (the first initial condition). $z(t)$ was described by the following periodic piecewise function

$$z(t) = \begin{cases} \dfrac{a_1 t^2}{2} & (0 \le t < t_1) \\[2mm] \dfrac{v_1{}^2}{2a_1} + v_1(t - t_1) & (t_1 \le t < t_2) \\[2mm] z_{max} + \dfrac{a_2(t-t_3)^2}{2} & (t_2 \le t < t_3) \\[2mm] z_{max} + \dfrac{a_3(t-t_3)^2}{2} & (t_3 \le t < t_4) \\[2mm] z_{max} + \dfrac{v_2{}^2}{2a_3} + v_2(t - t_4) & (t_4 \le t < t_5) \\[2mm] \dfrac{a_4(t-T)^2}{2} & (t_5 \le t < T) \\[2mm] z(t - T) & (t \ge T) \end{cases} \tag{12}$$

$$\text{with} \begin{cases} t_1 = \dfrac{v_1}{a_1} \\[2mm] t_2 = \dfrac{z_{max}}{v_1} + \dfrac{v_1}{2a_1} + \dfrac{v_1}{2a_2} \\[2mm] t_3 = \dfrac{z_{max}}{v_1} + \dfrac{v_1}{2a_1} - \dfrac{v_1}{2a_2} \\[2mm] t_4 = \dfrac{z_{max}}{v_1} + \dfrac{v_1}{2a_1} - \dfrac{v_1}{2a_2} + \dfrac{v_2}{a_3} \\[2mm] t_5 = \dfrac{z_{max}}{v_1} + \dfrac{v_1}{2a_1} - \dfrac{v_1}{2a_2} - \dfrac{z_{max}}{v_2} + \dfrac{v_2}{2a_3} + \dfrac{v_2}{2a_4} \\[2mm] T = \dfrac{z_{max}}{v_1} + \dfrac{v_1}{2a_1} - \dfrac{v_1}{2a_2} - \dfrac{z_{max}}{v_2} + \dfrac{v_2}{2a_3} - \dfrac{v_2}{2a_4} \end{cases} \tag{13}$$

Fig. 1(c) shows the air gap and the relative movement velocity between the top electrode and the electret film during one movement cycle defined by equation (12) and (13) using parameter values in Table 1. The period of one movement cycle (T) is 0.022s, and the top electrode moves at a speed of 0.1 or -0.1 m/s with reference to the electret film during 0.018s in one period. Fig. 1(d) shows the time-dependent total capacitance of the TENG (C_{TENG}) which is calculated by the following equation [30, 38]:

$$C_{TENG}(t) = \frac{C_f C_{gap}(t)}{C_f + C_{gap}(t)} = \frac{S\varepsilon_0}{(d_0 + z(t))} \tag{14}$$

. The total capacitance is an important factor that directly influences the output performance of TENG because the whole circuit of the TENG can be regarded as a resistor-capacitor (RC) series circuit constituted by the total capacitance and the load resistance. In equation (14), the fringe

effect is ignored since the side length of the TENG (3 inches) is much larger than the thickness of the electret film (125 μm) and the maximum air gap (1mm) used in our calculations. The maximum total capacitance (C_{max}), minimum total capacitance (C_{min}), and their ratio (C_{max}/C_{min}) have significant influences on the efficiency of TENG according to other researches [42, 43]. In our calculations, C_{max} is near 1398 pF, C_{max} is near 50 pF, and C_{max}/C_{min} is about 28.

4.2. The charge transfer process

Fig.2(a)~(c) show calculated charge transfer processes of the TENG in the first three movement cycles with a load resistance of 1 MΩ, 100 MΩ, and 1 GΩ respectively. Firstly, by comparing the R-related $Q(t)$ with the $Q_{eq}(t)$ which is only dependent on $z(t)$, it can be found that positive charges will transfer to the back electrode when $Q(t)<Q_{eq}(t)$, generating positive current. Here we defined that current is positive when positive charges transfer from the top electrode to the back electrode, with all results in this article based on the same definition. And when $Q(t)>Q_{eq}(t)$, positive charges will transfer in an opposite direction, generating negative current. The vertical dash-dot lines in Fig. 2(a)~(c) mark the moment when $Q(t)=Q_{eq}(t)$ and meanwhile $I(t)=0$. It can be summarized that the difference between $Q(t)$ and $Q_{eq}(t)$ leads to the charge transfer between the two electrodes in a direction that can reduce this difference.

Secondly, the first positive current peak (I_{pp1}) has an obviously larger amplitude than other current peaks. For example, I_{pp1} in Fig. 2(a) is ~36 μA, while the first negative current peak (I_{np1}) is ~-18.6 μA and the second positive current peak (I_{pp2}) is ~24.5 μA. This can be explained by characteristics of charging and discharging processes of the RC series circuit. For an RC series circuit, the charge or discharge time of the capacitor depends on the time constant ($\tau=R\times C$). With a larger τ, the charge or discharge takes longer time. For instance, in Fig. 2(b), at $t=0$, $Q(t)$, $Q_{eq}(t)$, and $|\Delta Q|$ (the difference between $Q(t)$ and $Q_{eq}(t)$) are 0, the C_{TENG} value is C_{max}. Then C_{TENG}

decreases but is still high, the $z(t)$-dependent $Q_{eq}(t)$ increases fast but the $Q(t)$ increases slower because of large τ with high C_{TENG}, making $|\Delta Q|$ increase. With C_{TENG} further decreasing, τ decreases a lot so that the charge can transfer faster, and $|\Delta Q|$ is gradually reduced to 0 at the time marked by the first vertical dash-dot line. After that, both $Q_{eq}(t)$ and $Q(t)$ decrease but C_{TENG} increases dramatically, resulting in an increasing τ and $|\Delta Q|$. When a whole movement cycle ends, $Q_{eq}(t)$ decreases to 0 but $Q(t)$ is still much larger than 0. Then $Q_{eq}(t)$ starts to increase again in the second movement cycle, τ starts to decrease, meanwhile $Q(t)$ keeps decreasing until the moment that $|\Delta Q|$ becomes 0 again as marked by the second vertical dash-dot line. Then the second charge transfer cycle begins. The charge transfer cycle (including an entire positive and an entire negative current peaks) lags the movement cycle, resulting in that transferred charge amount in the first positive current peak (Q_{trp1}) is larger than that in the first negative current peak (Q_{trn1}) and in following current peaks (Q_{trp2}, Q_{trn2}, Q_{trp3}…), making the first current peak higher than the others. In Fig. 2(b), I_{pp1} is ~4.8 µA, I_{np1} is ~-0.35 µA, and I_{pp2} is ~0.77 µA.

At last, in Fig. 2(a), the positive current peaks have a larger amplitude of ~24.5 µA than that of negative peaks of 18.6 µA in latter charge transfer cycles even with the same transferred charge amount ($Q_{trp2} = Q_{trn2} = Q_{trp3} =…$). And in Fig. 2(b) and (c), not only the amplitude and the area (physically meaning transferred charge amount Q_{trp}) of the positive current peaks (I_{pp}) are apparently larger than those of the negative ones (I_{np} and Q_{trn}), but also the time duration of the positive current peak (td_{pp}) is apparently longer than the negative one (td_{np}) in each charge transfer cycle. Moreover, it can be noticed from Fig. 2(b) and (c) that I_{pp} and td_{pp} gradually decrease from the first to the third charge transfer cycle, meanwhile the amplitude of I_{np} and td_{np} gradually increase. This asymmetric characteristic is also attributed to the lag between the charge transfer cycle and the movement cycle. And it becomes more obvious when R is larger since a

higher R leads to larger τ that heavily retards the charge transfer process. This will be further discussed in the following section 4.3.

4.3. Amplitude-variable outputs of the TENG with different load resistances

Fig. 3(a)~(c) show the calculated $Q(t)$, $I(t)$ and output voltage $V(t)$ of the TENG with different load resistances in the first 10 movement cycles. In Fig. 3(a), all $Q(t)$ calculated with different load resistances show smaller variation range than $Qeq(t)$ in each charge transfer cycle, and a higher R leads to a smaller variation range, meaning that fewer charge is transferred due to the larger resistance. With the resistance of 1 MΩ, 10 MΩ, and 100 MΩ, the variation of $Q(t)$ is limited in a stable range after three charge transfer cycles. Taking the charge transfer process with R of 100 MΩ as an example shown in Fig. 3(d), the amplitude of $Q(t)$ varies from the first to the third charge transfer cycles and then is limited between steady upper and lower limiting values marked by the red and black dash lines, respectively. This is because Q_{trp} is larger than Q_{trn} in the first and second charge transfer cycles and becomes the same with Q_{trn} at the third cycle as shown in the inset of Fig. 3(d). While with the resistance of 1 GΩ and 10 GΩ, the amplitude of $Q(t)$ keeps a growing trend in 10 movement cycles. In Fig.3(b), higher resistance leads to lower current amplitude, which is in good accordance with previous researches [30, 31]. Lower current amplitudes with higher resistances make the current peaks and their variations unobservable in Fig. 3(b). On the contrary, the output voltage is higher with higher resistance, making the variation in the amplitude of output voltages with higher resistances prominent as shown in Fig. 3(c). With the resistance of 1 MΩ, 10 MΩ, and 100 MΩ, the positive voltage peak value (V_{pp}) and the negative voltage peak value (V_{np}) vary to steady ranges in three cycles. With the high resistance as 1 GΩ and 10 GΩ, V_{pp} shows an apparent decreasing trend during all the ten cycles. All V_{pp} and V_{np} values with resistances of 100 MΩ, 1 GΩ, and 10 GΩ in the first ten

cycles are plotted in Fig. 3(e) and (f) respectively. We found that V_{pp} and V_{np} values vary with time perfectly in accordance with the following equation:

$$Vp(t) = V_s + V_a exp(-(t-t_0)/\tau_d) \tag{15}$$

, where t_0 is the time when the first corresponding voltage peak value (V_{pp1} for V_{pp} values, and V_{np1} for V_{np} values) appears, τ_d is a fitting parameter with the same unit of time, V_s and V_a are two other fitting parameters with the same unit of voltage. These parameter values are given in Table 2. All adjusted coefficients of determination of these fittings are 1, indicating perfect fittings. Standard errors of these parameters in fitting are given in Table S1 in the supporting information.

Table 2 Parameter values in fitting V_{pp} and V_{np} with the first initial condition

R Parameters	Fitting parameters for V_{pp}			Fitting parameters for V_{np}		
	100 MΩ	1 GΩ	10 GΩ	100 MΩ	1 GΩ	10 GΩ
V_s (V)	35.65	38.7	38.75	-38.36	-38.69	-38.7
t_0 (s)	0.007545	0.0108	0.01098	0.02198	0.022	0.022
V_a (V)	444	974.7	1079	3.856	30.75	37.82
τ_d (s)	0.009866	0.09574	0.9573	0.009573	0.09573	0.9573

The time-varying part in equation (15) has the same exponential form as the discharging curve equation of an RC circuit. In analogy with the RC circuit discharging process, we define the parameter τ_d as the time constant of this variation. We can find from Table 2 that τ_d is almost directly proportional to the resistance value R especially for the high R of 1 GΩ and 10 GΩ, and the proportionality coefficient is about 9.57×10^{-11} for both V_{pp} and V_{np} fittings, meaning that it takes longer time for the TENG to give steady output with higher R than with lower R. From equation (15), it can be inferred that the V_{pp} or V_{pp} value will gradually approach the corresponding V_s (steady peak voltage) value when the time is long enough. By using equation

(15) and parameters' values in Table 2, V_{pp} and V_{np} values in 6 seconds were calculated and shown in Fig. 3(g). Though the first V_{pp} and V_{np} values with 100 MΩ, 1 GΩ, and 10 GΩ are so different as shown in Fig. 3(e) and (f), after 6 seconds, their difference becomes very small since the V_s values with 100 MΩ, 1 GΩ, and 10 GΩ are very close, as given in Table 2. The parameter V_a determines the difference between the V_{pp1} or V_{np1} and the corresponding V_s, which determines rangeability of V_{pp} or V_{np}. In Table 2, V_a is larger with larger resistance for both V_{pp} and V_{np}, meaning that rangeability of V_{pp} or V_{np} is larger with higher resistance.

Calculated V_{pp1}, V_{np1}, and V_{np10} with different resistances are shown in Fig. 3(h) and (i). Both V_{pp1} and V_{pp10} increase with increasing R and saturate at a value of ~1130 V when R is high enough, while the absolute values of V_{np1}, and V_{np10} increase with R from 1 MΩ to 100 MΩ and then decrease with increasing R.

Besides the transferred charge, output current, and output voltage, the output power is the most important to evaluate the performance of the TENG. Fig. 4(a) shows the calculated time-dependent output power $P(t)$ of the TENG with different load resistances in the first 10 movement cycles by the following equation:

$$P(t) = I^2(t)R \tag{16}$$

. In the first movement cycle, the maximum peak $P(t)$ increases from ~1.29 mW to ~2.30 mW when R increases from 1 MΩ to 100 MΩ, and then decreases to ~0.125 mW when R further increases 10 GΩ. However, in following movement cycles, $P(t)$ peak values are much lower than those in the first cycle, especially for $P(t)$ with R of 10 MΩ and 100 MΩ. This can also be noticed from Fig.4(b) that presents the output energy $W(t)$ of the TENG to different load resistance based on the following equation:

$$W(t) = \int_0^t P(t)dt \tag{17}$$

. Though the output energy with R of 100 MΩ after the first movement cycle is much higher than those with other resistances, in following cycles little energy is output with R of 100 MΩ and the total energy is overpassed by that with R of 1 GΩ after several cycles. The average output power ($AvgP$) of the TENG in each movement cycle can be calculated by the following equation:

$$AvgP(c) = \frac{\int_{(c-1)*T}^{c*T} P(t)dt}{T} \tag{18}$$

, where c is the movement cycle number and T is the period of the movement given in the equation (13). As shown in Fig. 4(c), in the first cycle, the TENG outputs the highest average power of ~806 μW with R of 100 MΩ among calculated resistances. But at the tenth cycle, the $AvgP$ with R of 1 MΩ is the highest as ~45 μW, and the $AvgP$ with R of 100 MΩ becomes the lowest as ~5.6 μW among all calculated values. The first $P(t)$ peak values and $AvgP$ values at the first and the tenth cycles with different load resistances are plotted in Fig. 4(d) for better comparison.

4.4. Calculation with another initial condition

Then the case $z(0) = z_{max}$ and $Q(0) = Q_{max}$ was considered (the second initial condition), using the same parameter values in Table 1. The time-dependent z(t) and the relative movement velocity between the top electrode and the electret film during one movement cycle are plotted in Fig. S2 in the supporting information.

Fig. 5(a)~(c) shows the calculated charge transfer process of the TENG in the first three movement cycles with a load resistance of 1 MΩ, 100 MΩ, and 1 GΩ, respectively. The first current peak is negative due to the moving direction is opposite to that in Fig. 2, and the

amplitude of the first current peak (I_{np1}) shows a smaller difference with other current peaks than in Fig. 2. For instance, in Fig. 5(a), the first to the third negative current peaks have the same value of ~-18.6 μA, and the first to the third negative current peaks have the same value of ~24.5 μA. Moreover, in Fig. 5(b) and (c), the amplitude of I_{np} is higher than that of I_{pp}, but their difference is also smaller than that in Fig. 2(b) and (c). This is also due to variations of C_{TENG} and $|\Delta Q|$. For instance, in Fig. 5(b), in the time duration of the first negative current peak (td_{np1}), both the maximum $|\Delta Q|$ and C_{TENG} are much larger than those in the time duration of the first positive current peak (td_{pp1}). So even though the transferred charge amount in the time duration of td_{np1} is larger, it takes longer time to complete the charge transfer than that in the time duration of td_{pp1} (meaning $td_{np1}>td_{pp1}$), which contributes to making the difference between the amplitude of I_{np} and I_{pp} less than that in Fig.2. In addition, it can be noticed from Fig. 5(b) and (c) that the amplitude of I_{np} and td_{np} gradually decrease from the first to the third charge transfer cycle, meanwhile I_{pp} and td_{pp} gradually increase.

Fig. 6(a)~(c) show the calculated $Q(t)$, $I(t)$ and $V(t)$ of the TENG with different load resistances in the first 10 movement cycles using the second initial condition. Variations in the amplitude of $Q(t)$ and $I(t)$ with high R are not easy to observe in Fig. 6(a) and (b), but the variation in the amplitude of $V(t)$ can be clearly noticed in Fig. 6(c). In comparison with Fig. 3(c), it's similar that the amplitude of $V(t)$ varies at first and then goes to near-stable ranges in three cycles with R of 1 MΩ, 10 MΩ, and 100 MΩ, but it keeps varying even after ten cycles with higher R of 1 GΩ and 10 GΩ. V_{pp} and V_{np} values also vary with time perfectly in accordance with equation (15). The parameter values in fitting V_{pp} and V_{pp} in Fig. 6(c) are given in Table 3. Standard errors of these parameters in fitting are given in Table 2S in the supporting information.

Table 3 Parameters values used in fitting V_{pp} and V_{np} with the second initial condition

R ╲ Parameters	Fitting parameters for V_{pp}			Fitting parameters for V_{np}		
	100 MΩ	1 GΩ	10 GΩ	100 MΩ	1 GΩ	10 GΩ
V_s (V)	35.66	38.66	38.71	-38.36	-38.69	-38.7
t_0 (s)	0.02116	0.02198	0.022	0.01095	0.011	0.011
V_a (V)	-3.743	-30.73	-37.83	-0.3658	-1.221	-1.357
τ_d (s)	0.009562	0.09568	0.9578	0.009549	0.09573	0.9573

V_s values in Table 3 are almost the same with those in Table 2, meaning that peak values of $V(t)$ of the TENG with these two different initial conditions will finally be the same. V_a values in Table 3 are all negative, meaning that the amplitude of the positive voltage peak ($|V_{pp}|$) gradually increases but that of negative voltage peak ($|V_{np}|$) decreases with the cycle number. Each $|V_a|$ is smaller than the corresponding one in Table 2, reflecting the fact that variation ranges in the amplitude of $V(t)$ in Fig. 6(c) are smaller than those in Fig. 3(c) with the same R. And the time constant τ_d values in Table 3 are almost the same with those corresponding in Table 2. Fig. 6(d) shows $V(t)$ in the first 25 movement cycles of the TENG with R of 1 GΩ as an example. The amplitude of positive voltage peaks shows an apparent increasing trend and then approaches to a steady value, while the amplitude of negative voltage peaks slightly decreases and then approaches to a steady value. And the variation of $V(t)$ is limited between the fitted lines for V_{pp} and V_{np} using the values of parameters given in Table 3.

The output voltage peak values with this initial condition are plotted in Fig. 6(e) and (f). For positive voltage peaks, both the V_{pp1} and V_{pp10} firstly increase with R from 1 MΩ to 100 MΩ, and then both decrease with higher R. Nevertheless, the final steady V_{pp} value shows a monotone increasing trend with R. For the negative voltage peaks, the amplitude of V_{np1}, V_{np10} and steady V_{np} values all monotonically increase with R from 1 MΩ to 10 GΩ. To be more explicit, the

steady V_{pp} and V_{np} values with R of 100 MΩ, 1 GΩ, and 10 GΩ are estimated from the corresponding V_s values in Table 3.

Fig. 7(a)~(c) present the output power, energy, and average power per movement cycle of the TENG in the first 10 movement cycles, using with the second initial condition. The influence of R on the output power and average power is shown in Fig. 7(d). In all movement cycles, lower R leads to both higher peak power and average power, which is different from the result shown in Fig. 4. Values of the output power peak and the average power in the first movement cycle with different R are lower than those in Fig. 4(d). More similarities and differences in the output energy and power of the TENG calculated from these two initial conditions are discussed in section 4.5.

4.5. QV cycles and the optimum load resistance

The output energy of the TENG can be explicitly evaluated from the charge-voltage (QV) cycle diagram. Fig. 8(a) an (b) show the QV cycles of the TENG during no less than 10 movement cycles calculated from the first and the second initial conditions respectively. The area of the QV loop equals the output energy of the TENG per charge transfer cycle [44]. In Fig. 8(a), with relatively low R as 1 MΩ, 10 MΩ, and 100 MΩ, the QV line shows a large span semi-circular arc shape during the first charge transfer cycle and then becomes a closed loop in less than 3 movement cycles, while for the results with high R as 1 GΩ, and 10 GΩ, the QV line keeps unclosed with a damped variation trend in calculated 30 movement cycles. In Fig. 8(b), with R of 1 MΩ, 10 MΩ, and 100 MΩ, there is no span semi-circular arc-shaped line and the QV line becomes a closed loop in less than 3 movement cycles, while with higher R as 1 GΩ, and 10 GΩ, the QV line keeps unclosed with a growing variation trend in calculated 25 movement cycles. The area of the QV cycle with R of 1 MΩ in Fig. 8(b) is the largest as ~ 0.99 μJ per cycle

among those with all the calculated resistances, which is also in accordance with the results presented in Fig. 7(b)~(d).

For a better comparison, the Q-V data calculated with these two different initial conditions with R of 1 MΩ, 100 MΩ, and 1 GΩ were plotted in Fig. 8(c)-(e) respectively. Fig. 8(c) and (d) demonstrate the results of the first 10 movement cycles from the first initial condition (from 0) and the first 10 cycles from the second initial condition (from Q_{max}). The QV cycles determined by the two initial conditions become overlapped after the first cycle with R of 1 MΩ, and it takes about three cycles for those with R of 100 MΩ to become overlapped. In Fig. 8(e) with the data of the first 100 cycles from the first and second initial conditions, both QV cycles get closer and closer but not overlap at least in the first 25 cycles. Fig. S3 in the supporting information clearly shows that the 100th QV cycles of the TENG with R of 1 GΩ starting from these two initial conditions overlap with each other. In addition, Fig. S4 in the supporting information indicates that the TENG finally outputs the same QV diagram using another initial condition $z(0) = z_{max}/2$ and $Q(0) = Q_{eq}(0)$. We can infer from these results that the QV cycle of a TENG driven by steady periodic movement cycles will finally become a specific steady closed loop with a specific R and periodic driving movement after long enough time (when Q_{trp} equals Q_{trn} as shown in the inset of Fig. 3(d)), and it takes longer time for the TENG to output the steady QV cycle if with enough higher R than with lower R. It should be noticed that all these results are calculated on the basis that the movement is continuous without pause, otherwise, with pause among the contact and separation, the output power of the TENG that starts working from the first initial condition will probably have larger output power since the charge transfer can be more complete during the pause in the contact state.

To get the more accurate optimum load resistance that making the TENG output the maximum steady $AvgP$, the $AvgP$ in the third movement cycle of the TENG with R from 0.5 MΩ to 2 MΩ were calculated by using the second initial condition and shown in Fig. 8(f). The $AvgP$ increases and then decreases with increasing R and gets the maximum value of ~45.27 μW with R of 1.2 MΩ among the calculated data.

5. Experimental verification

To verify the calculated results above, a TENG using a 4 cm × 4 cm sized 100 μm-thick PTFE film (ε_r=2.1) as the triboelectric-electret layer was measured according to details given in section 2.2. Values of parameters for movement (z_{max}, v_1, v_2, a_1, a_2, a_3, and a_4) were set in the control software of the linear motor as values listed in Table 1. However, due to the complexity of real forces caused by the strike, vibration, or imprecise control during the movement of the slider block of the linear motor, the recorded values of movement parameters are slightly different from the set ones. Fig. 9(a) and (b) show z-t and v-t data recorded by the control software of the linear motor. The actual maximum air gap is about 0.7 mm during the movement of the slider block, and the maximum speed in two directions is about 0.14 m/s and -0.17 m/s respectively. The slider block keeps almost still for ~0.011 s when it moves to the position of z=0, and it moves at rather low velocity for ~0.011 s when it gets close to the position of z=0.7 mm. To simplify the calculation, the movement velocity during these two durations of 0.011 s was set as 0, and these two durations were named the waiting time t_{w1} and t_{w2}. The acceleration and deceleration of the slider block were estimated according to the fitting results of the v-t data as shown in Fig. S5 and S6 in the supporting information. To estimate the charge density on the PTFE film, the transfer charge amount of the TENG was measured, with setting the z_{max} as 10 mm and the slider block keeps still for 5 s when it moves to both positions of z=0 and z=z_{max}.

With such a large z_{max} and still duration, it's reasonable to assume that the short-circuit transferred charge amount approximates to the charge amount on the PTFE film [29, 45]. From the measured transferred charge results shown in Fig. 9(c), the polarity of charges on the PTFE film was confirmed to be negative since positive charges were transferred from the top electrode to the back electrode during the separation process, and in the opposite direction when the top electrode approaches the electret film. And the charge density of the PTFE film was estimated around -50 μC/m^2, according to the measured maximum transferred charge amount of ~80 nC for a 4 cm $\times$ 4 cm sized PTFE film.

The measured output voltages of the TENG with the load resistance of 10 MΩ, 100 MΩ, and 1.1 GΩ are plotted in Fig. 9(d)~(f). And the calculated output voltages of the TENG with corresponding load resistances are presented in Fig. 9(g)~(i). The parameter values for calculations are set according to measured data in Fig. 9(a)~(c) and listed in Table 4. The $z(t)$, $v(t)$, and $C_{TENG}(t)$ data using these parameter values are shown in Fig. S4 in the supporting information. With R of 10 MΩ, both the calculated and measured output voltages have no apparent variation in the peak amplitude for both initial conditions. With R of 100 MΩ, the first positive voltage peak of both the calculated and measured output voltages using the first initial condition has a much larger amplitude than other peaks. And with R of 1.1 GΩ, apparent variations in the amplitude of voltage peaks appear both in the experimental and calculated data during several movement cycles, especially for the result using the first initial condition, and then the amplitude of voltage peaks becomes almost the same for both initial conditions. These results confirm the presence of variations in the amplitude of output voltages of the TENG with high load resistances and reveal the influence of the initial condition and the load resistance on the output of the TENG.

Table 4. Parameter values in calculating the output of TENG for experimental validation

Parameter	Value
S	16 cm^2
ε_r	2.1
d_f	100 μm
σ	50 μC/m^2
Maximum gap z_{max}	0.7 mm
Maximum speed v_1	0.14 m/s
Maximum speed v_2	-0.17 m/s
Acceleration a_1	33 m/s^2
Deceleration a_2	-33 m/s^2
Waiting time t_{w1}	0.11 s
Deceleration a_3	-50 m/s^2
Acceleration a_4	50 m/s^2
Waiting time t_{w1}	0.11 s
Waiting time t_{w2}	0.11 s

6. Conclusions

In conclusion, we used symbolic computations in MATLAB to calculate the charge transfer process and output current/voltage/power of a TENG driven by a piecewise periodic reciprocating movement with acceleration/deceleration processes, with a load resistance of 1 MΩ, 10 MΩ, 100 MΩ, 1 GΩ, and 10 GΩ, respectively. It is found that the amplitude of the output current/voltage of the TENG varies over time in an exponential form, resulting from the lag between the charge transfer cycle and the movement cycle. This lag also leads to the asymmetric characteristics between the output positive and negative current/voltage peaks. The larger the load resistance is, the longer time it takes for the TENG to get steady output. When the TENG starts working from the contact position, the variation range of the output voltage peaks is larger than that when the TENG starts working from the fully-separated position, despite the same load resistance, and the average output power and the optimum load resistance of the TENG in the steady output range are quite different from those in the first working cycle. It is also found that

the TENG finally outputs the same steady QV cycle with the same load resistance and periodical driving movement after long enough time. Moreover, the variations in the output voltage peaks of a PTFE film-based TENG with different load resistances and initial conditions were confirmed by both experiments and calculations. It is worth mentioning that, for comparison with other works [31, 38], regular periodic movements are used for the calculations in this work. External movements provided by a human (such as finger presses) and other moving objects (cars, trains, flags, etc.) are mostly irregular and more complicated. Nevertheless, our results remind that the match between the charge transfer characteristics (which can be regulated by the TENG structure parameters such as the electret film thickness, or by the power management circuit) and the mechanical source characteristics (such as frequency) should be considered in building efficient TENG-powered systems.

Acknowledgments

References

[1] F.R. Fan, Z.Q. Tian, Z.L. Wang, Flexible triboelectric generator!, Nano Energy, 1 (2012) 328-334. https://doi.org/10.1016/j.nanoen.2012.01.004

[2] Z.L. Wang, Triboelectric nanogenerators as new energy technology for self-powered systems and as active mechanical and chemical sensors, ACS Nano, 7 (2013) 9533-9557. https://doi.org/10.1021/nn404614z

[3] G. Zhu, Z.-H. Lin, Q. Jing, P. Bai, C. Pan, Y. Yang, Y. Zhou, Z.L. Wang, Toward large-scale energy harvesting by a nanoparticle-enhanced triboelectric nanogenerator, Nano Lett., 13 (2013) 847-853. https://doi.org/10.1021/nl4001053

[4] T. Zhou, L. Zhang, F. Xue, W. Tang, C. Zhang, Z.L. Wang, Multilayered electret films based triboelectric nanogenerator, Nano Res., 9 (2016) 1442-1451. https://doi.org/10.1007/s12274-016-1040-y

[5] Q. Zhong, J. Zhong, B. Hu, Q. Hu, J. Zhou, Z.L. Wang, A paper-based nanogenerator as a power source and active sensor, Energy Environ. Sci., 6 (2013) 1779-1784. https://doi.org/10.1039/c3ee40592c

[6] J. Zhong, Y. Zhang, Q. Zhong, Q. Hu, B. Hu, Z.L. Wang, J. Zhou, Fiber-based generator for wearable electronics and mobile medication, ACS Nano, 8 (2014) 6273-6280. https://doi.org/10.1021/nn501732z

[7] Z.L. Wang, T. Jiang, L. Xu, Toward the blue energy dream by triboelectric nanogenerator networks, Nano Energy, 39 (2017) 9-23. https://doi.org/10.1016/j.nanoen.2017.06.035

[8] Z.L. Wang, J. Chen, L. Lin, Progress in triboelectric nanogenerators as a new energy technology and self-powered sensors, Energy Environ. Sci., 8 (2015) 2250-2282. https://doi.org/10.1039/c5ee01532d

[9] H. Ryu, J.H. Lee, U. Khan, S.S. Kwak, R. Hinchet, S.-W. Kim, Sustainable direct current powering triboelectric nanogenerator via intent asymmetrical design, Energy Environ. Sci., (2018). https://doi.org/10.1039/C8EE00188J

[10] S. Meninger, J.O. Mur-Miranda, R. Amirtharajah, A. P. Chandrakasan, J.H. Lang, Vibration-to-electric energy conversion, IEEE Trans. Very Large Scale Integr. VLSI Syst., 9 (2001) 64-76. https://doi.org/10.1109/92.920820

[11] W. Du, X. Han, L. Lin, M. Chen, X. Li, C. Pan, Z.L. Wang, A three dimensional multi-layered sliding triboelectric nanogenerator, Adv. Energy Mater., 4 (2014) 1301592. https://doi.org/10.1002/aenm.201301592

[12] Q. Zheng, B. Shi, F. Fan, X. Wang, L. Yan, W. Yuan, S. Wang, H. Liu, Z. Li, Z.L. Wang, In vivo powering of pacemaker by breathing-driven implanted triboelectric nanogenerator, Adv. Mater., 26 (2014) 5851-5856. https://doi.org/10.1002/adma.201402064

[13] L.B. Huang, W. Xu, G.X. Bai, M.C. Wong, Z.B. Yang, J.H. Hao, Wind energy and blue energy harvesting based on magnetic-assisted noncontact triboelectric nanogenerator, Nano Energy, 30 (2016) 36-42. https://doi.org/10.1016/j.nanoen.2016.09.032

[14] H. Zhang, S. Feng, D. He, Y. Xu, M. Yang, J. Bai, An electret film-based triboelectric nanogenerator with largely improved performance via a tape-peeling charging method, Nano Energy, 48 (2018) 256-265. https://doi.org/10.1016/j.nanoen.2018.03.051

[15] Y. Yang, H. Zhang, X. Zhong, F. Yi, R. Yu, Y. Zhang, Z.L. Wang, Electret film-enhanced triboelectric nanogenerator matrix for self-powered instantaneous tactile imaging, ACS Appl. Mater. Interfaces, 6 (2014) 3680-3688. https://doi.org/10.1021/am406018h

[16] Z.L. Wang, Triboelectric nanogenerators as new energy technology and self-powered sensors–principles, problems and perspectives, Faraday Discuss., 176 (2015) 447-458. https://doi.org/10.1039/C4FD00159A

[17] F.-R. Fan, L. Lin, G. Zhu, W. Wu, R. Zhang, Z.L. Wang, Transparent triboelectric nanogenerators and self-powered pressure sensors based on micropatterned plastic films, Nano Lett., 12 (2012) 3109-3114. https://doi.org/10.1021/nl300988z

[18] X. Wang, H. Zhang, L. Dong, X. Han, W. Du, J. Zhai, C. Pan, Z.L. Wang, Self-powered high-resolution and pressure-sensitive triboelectric sensor matrix for real-time tactile mapping, Adv. Mater., 28 (2016) 2896-2903. https://doi.org/10.1002/adma.201503407

[19] F. Yi, L. Lin, S. Niu, J. Yang, W. Wu, S. Wang, Q. Liao, Y. Zhang, Z.L. Wang, Self-powered trajectory, velocity, and acceleration tracking of a moving object/body using a triboelectric sensor, Adv. Funct. Mater., 24 (2014) 7488-7494. https://doi.org/10.1002/adfm.201402703

[20] A. Yu, M. Song, Y. Zhang, Y. Zhang, L. Chen, J. Zhai, Z.L. Wang, Self-powered acoustic source locator in underwater environment based on organic film triboelectric nano-generator, Nano Res., 8 (2015) 765-773. https://doi.org/10.1007/s12274-014-0559-z

[21] B. Wang, J. Zhong, Q. Zhong, N. Wu, X. Cheng, W. Li, K. Liu, L. Huang, B. Hu, J. Zhou, Sandwiched composite fluorocarbon film for flexible electret generator, Adv. Electron. Mater., 2 (2016) 1500408. https://doi.org/10.1002/aelm.201500408

[22] M.L. Seol, J.H. Woo, S.B. Jeon, D. Kim, S.J. Park, J. Hur, Y.K. Choi, Vertically stacked thin triboelectric nanogenerator for wind energy harvesting, Nano Energy, 14 (2015) 201-208. https://doi.org/10.1016/j.nanoen.2014.11.016

[23] J. Ryu, J.E. Kang, Y. Zhou, S.Y. Choi, W.H. Yoon, D.S. Park, J.J. Choi, B.D. Hahn, C.W. Ahn, J.W. Kim, Y.D. Kim, S. Priya, S.Y. Lee, S. Jeong, D.Y. Jeong, Ubiquitous magneto-mechano-electric generator, Energy Environ. Sci., 8 (2015) 2402-2408. https://doi.org/10.1039/c5ee00414d

[24] Z.C. Quan, C.B. Han, T. Jiang, Z.L. Wang, Robust thin films-based triboelectric nanogenerator arrays for harvesting bidirectional wind energy, Adv. Energy Mater., 6 (2016) 1501799. https://doi.org/10.1002/aenm.201501799

[25] C. Zhang, W. Tang, C. Han, F. Fan, Z.L. Wang, Theoretical comparison, equivalent transformation, and conjunction operations of electromagnetic induction generator and triboelectric nanogenerator for harvesting mechanical energy, Adv. Mater., 26 (2014) 3580-3591. https://doi.org/10.1002/adma.201400207

[26] Y. Naruse, N. Matsubara, K. Mabuchi, M. Izumi, S. Suzuki, Electrostatic micro power generation from low-frequency vibration such as human motion, J. Micromech. Microeng., 19 (2009) 094002. https://doi.org/10.1088/0960-1317/19/9/094002

[27] Y. Arakawa, Y. Suzuki, N. Kasagi, Micro seismic power generator using electret polymer film, Proc. PowerMEMS, (2004) 187-190. https://doi.org/10.1299/jsmepes.2004.9.37

[28] Y. Suzuki, D. Miki, M. Edamoto, M. Honzumi, A mems electret generator with electrostatic levitation for vibration-driven energy-harvesting applications, J. Micromech. Microeng., 20 (2010) 104002. https://doi.org/10.1088/0960-1317/20/10/104002

[29] Y. Zi, S. Niu, J. Wang, Z. Wen, W. Tang, Z.L. Wang, Standards and figure-of-merits for quantifying the performance of triboelectric nanogenerators, Nat. Commun., 6 (2015) 8376. https://doi.org/10.1038/ncomms9376

[30] S. Niu, Z.L. Wang, Theoretical systems of triboelectric nanogenerators, Nano Energy, 14 (2015) 161-192. https://doi.org/10.1016/j.nanoen.2014.11.034

[31] S. Niu, S. Wang, L. Lin, Y. Liu, Y.S. Zhou, Y. Hu, Z.L. Wang, Theoretical study of contact-mode triboelectric nanogenerators as an effective power source, Energy Environ. Sci., 6 (2013) 3576-3583. https://doi.org/10.1039/c3ee42571a

[32] S. Niu, Y. Liu, Y.S. Zhou, S. Wang, L. Lin, Z.L. Wang, Optimization of triboelectric nanogenerator charging systems for efficient energy harvesting and storage, IEEE Trans. Electron Devices, 62 (2015) 641-647. https://doi.org/10.1109/ted.2014.2377728

[33] S. Niu, Y. Liu, S. Wang, L. Lin, Y.S. Zhou, Y. Hu, Z.L. Wang, Theoretical investigation and structural optimization of single-electrode triboelectric nanogenerators, Adv. Funct. Mater., 24 (2014) 3332-3340. https://doi.org/10.1002/adfm.201303799

[34] S. Niu, Y. Liu, X. Chen, S. Wang, Y.S. Zhou, L. Lin, Y. Xie, Z.L. Wang, Theory of freestanding triboelectric-layer-based nanogenerators, Nano Energy, 12 (2015) 760-774. https://doi.org/10.1016/j.nanoen.2015.01.013

[35] S. Boisseau, G. Despesse, A. Sylvestre, Optimization of an electret-based energy harvester, Smart Mater. Struct., 19 (2010) 075015. https://doi.org/10.1088/0964-1726/19/7/075015

[36] G.M. Sessler, Electrostatic microphones with electret foil, J. Acoust. Soc. Am., 35 (1963) 1354-1357. https://doi.org/10.1121/1.1918697

[37] S. Boisseau, G. Despesse, T. Ricart, E. Defay, A. Sylvestre, Cantilever-based electret energy harvesters, Smart Mater. Struct., 20 (2011) 105013. https://doi.org/10.1088/0964-1726/20/10/105013

[38] R. Hinchet, A. Ghaffarinejad, Y. Lu, J.Y. Hasani, S.-W. Kim, P. Basset, Understanding and modeling of triboelectric-electret nanogenerator, Nano Energy, 47 (2018) 401-409. https://doi.org/10.1016/j.nanoen.2018.02.030

[39] R.D.I.G. Dharmasena, K.D.G.I. Jayawardena, C.A. Mills, J.H.B. Deane, J.V. Anguita, R.A. Dorey, S.R.P. Silva, Triboelectric nanogenerators: Providing a fundamental framework, Energy Environ. Sci., 10 (2017) 1801-1811. https://doi.org/10.1039/C7EE01139C

[40] K. Dai, X. Wang, S. Niu, F. Yi, Y. Yin, L. Chen, Y. Zhang, Z. You, Simulation and structure optimization of triboelectric nanogenerators considering the effects of parasitic capacitance, Nano Res., 10 (2017) 157-171. https://doi.org/10.1007/s12274-016-1275-7

[41] B. Yang, W. Zeng, Z.H. Peng, S.R. Liu, K. Chen, X.M. Tao, A fully verified theoretical analysis of contact‐mode triboelectric nanogenerators as a wearable power source, Adv. Energy Mater., 6 (2016) 1600505. https://doi.org/10.1002/aenm.201600505

[42] A. Karami, D. Galayko, P. Basset, Characterization of the capacitance variation of electrostatic vibration energy harvesters biased following rectangular charge-voltage diagrams, J. Phys.: Conf. Ser., 773 (2016) 012015. https://doi.org/10.1088/1742-6596/773/1/012015

[43] Y. Lu, E. O'Riordan, F. Cottone, S. Boisseau, D. Galayko, E. Blokhina, F. Marty, P. Basset, A batch-fabricated electret-biased wideband mems vibration energy harvester with frequency-up conversion behavior powering a UHF wireless sensor node, J. Micromech. Microeng., 26 (2016) 124004. https://doi.org/10.1088/0960-1317/26/12/124004

[44] D. Galayko, E. Blokhina, P. Basset, F. Cottone, A. Dudka, E.O. Riordan, F. Orla, Tools for analytical and numerical analysis of electrostatic vibration energy harvesters: Application to a continuous mode conditioning circuit, J. Phys.: Conf. Ser., 476 (2013) 012076. https://doi.org/10.1088/1742-6596/476/1/012076

[45] S. Wang, Y. Xie, S. Niu, L. Lin, C. Liu, Y.S. Zhou, Z.L. Wang, Maximum surface charge density for triboelectric nanogenerators achieved by ionized‑air injection: Methodology and theoretical understanding, Adv. Mater., 26 (2014) 6720-6728. https://doi.org/10.1002/adma.201402491
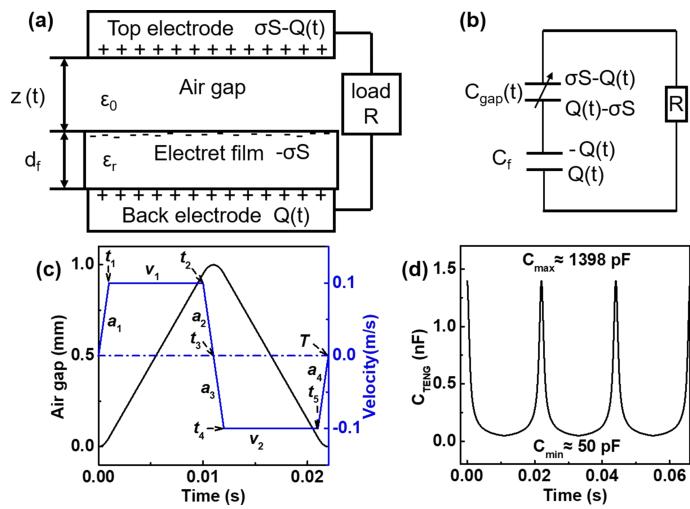
Fig.1. (a) The cross-section structure of the triboelectric-electret nanogenerator (TENG). (b) The simplified equivalent circuit model of the TENG. (c) The time-dependent air gap, velocity-v, acceleration/deceleration-a, and (d) total capacitance of the TENG (C_{TENG}).
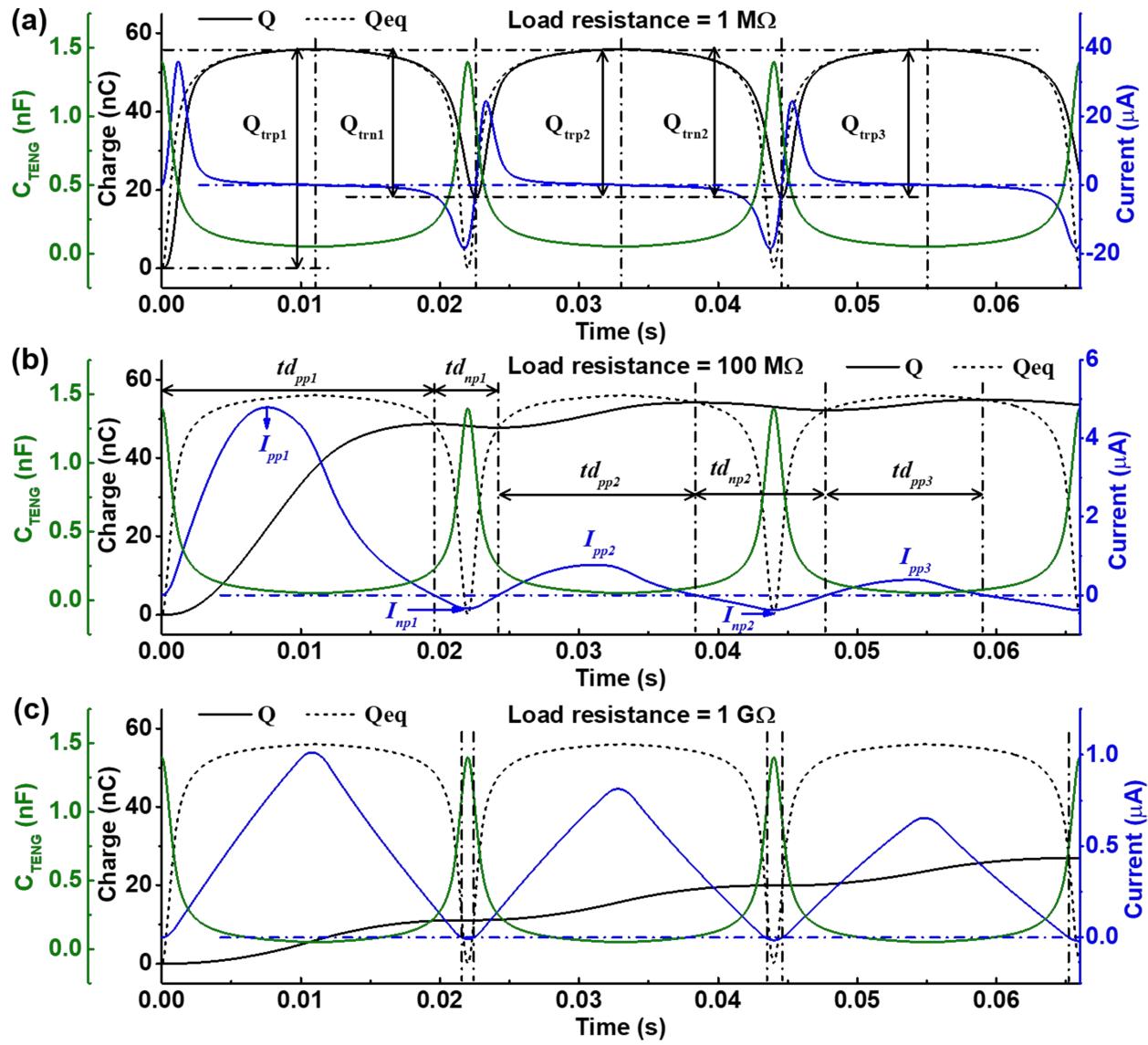
Fig.2. Charge transfer processes of the TENG calculated with the load resistances of (a) 1 MΩ, (b) 100 MΩ, and (c) 1 GΩ, using the initial condition that the TENG starts working from the contact position.
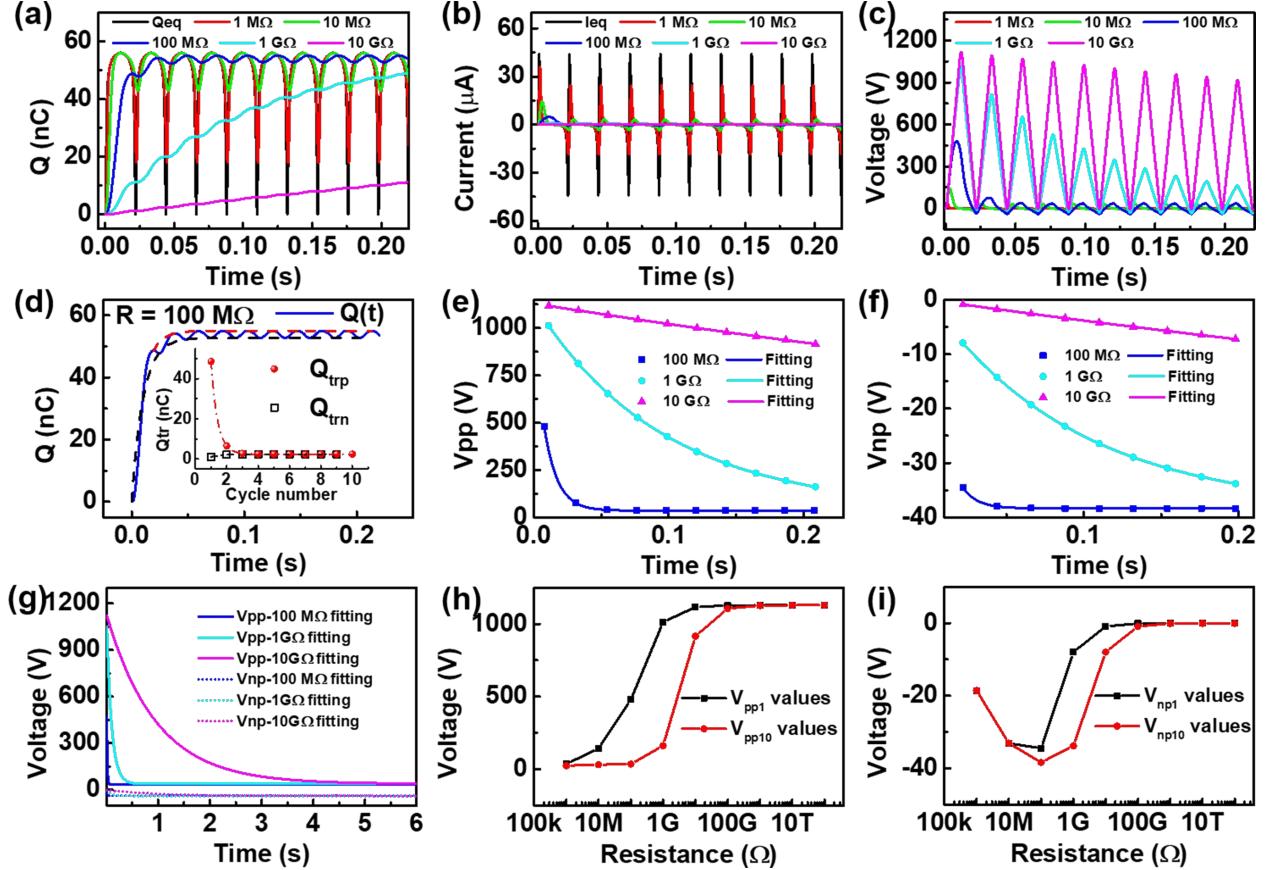
**Fig.3.** Output characteristics of the TENG calculated with the different load resistances during 10 movement cycles, using the initial condition that the TENG starts working from the contact position. (a) Time-dependent $Q(t)$, (b) $I(t)$, and (c) $V(t)$ of the TENG. (d) The variation in the amplitude of $Q(t)$, with inset showing the variation in transferred charge amounts in two directions (Q_{trp} and Q_{trn}). (e) Positive (V_{pp}) and (f) negative (V_{np}) voltage peak values with fitted curves. (g) Fitted variation trend of V_{pp} and V_{np} in 6s. (h) V_{pp1} and V_{pp10} values with different load resistances. (i) V_{np1} and V_{np10} values with different load resistances.
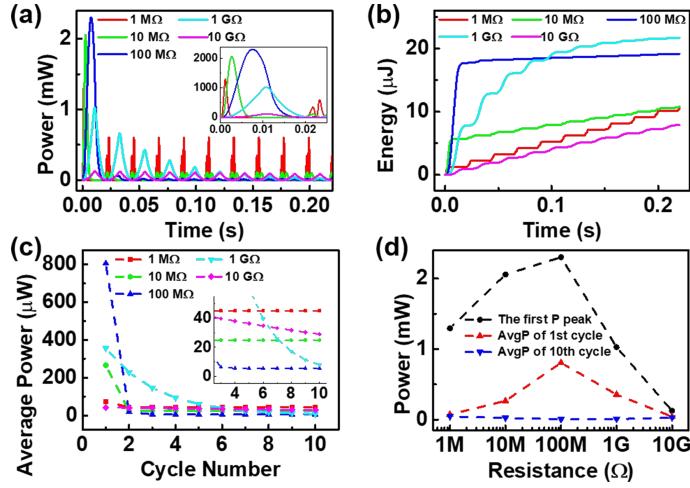
Fig.4. Output power and energy of the TENG calculated with the different load resistances during the first ten movement cycles, using the initial condition that the TENG starts working from the contact position. (a) Instantaneous output power (*P(t)*) of the TENG. (b) Time-dependent output energy (*W(t)*) of the TENG. (c) Average output power per movement cycle (*AvgP*) of the TENG. (d) The first *P(t)* peak value, and the *AvgP* in the first and tenth movement cycles of the TENG with different load resistances.
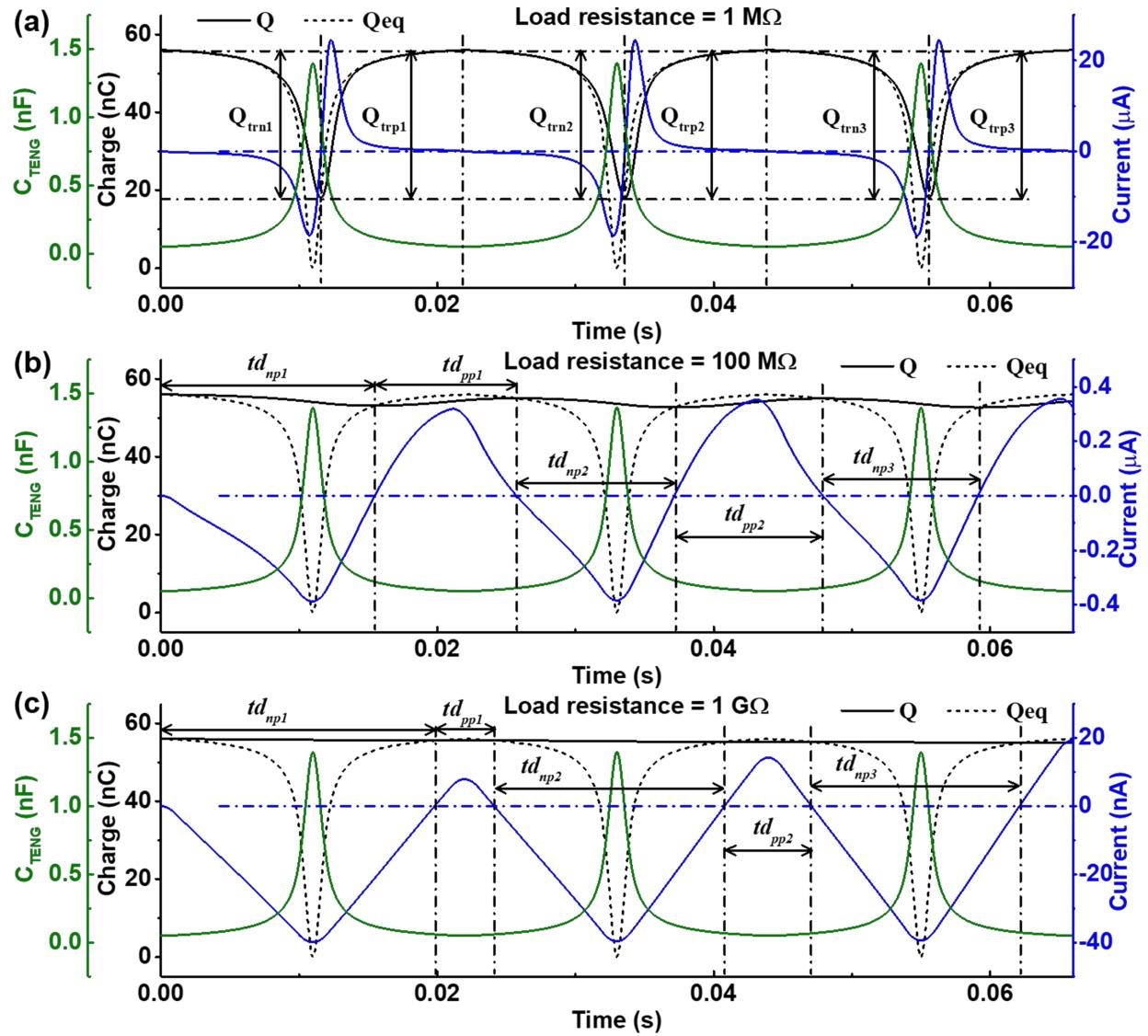
Fig.5. Charge transfer processes of the TENG calculated with the load resistances of (a) 1 MΩ, (b) 100 MΩ, and (c) 1 GΩ, using the initial condition that the TENG starts working from the separated position.
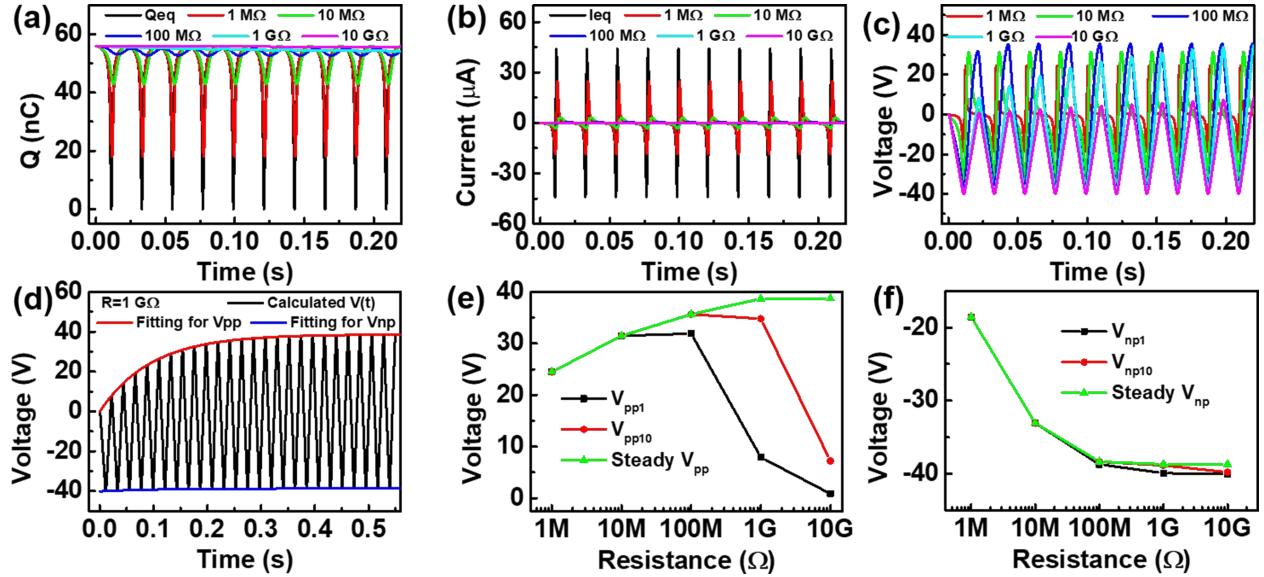
Fig.6. Output characteristics of the TENG calculated with the different load resistances during the first 10 movement cycles, using the initial condition that the TENG starts working from the separated position. (a) Time-dependent $Q(t)$, (b) $I(t)$, and (c) $V(t)$ of the TENG. (d) Output $V(t)$ of the TENG with a load resistance of 1 GΩ during 25 movement cycles, with the variation trend in the amplitude of $V(t)$ marked by fitted curves for output voltage peak values. (e) Positive (V_{pp}) and (f) negative (V_{np}) voltage peak values of the TENG with different load resistances during the first and tenth movement cycles and their steady values.
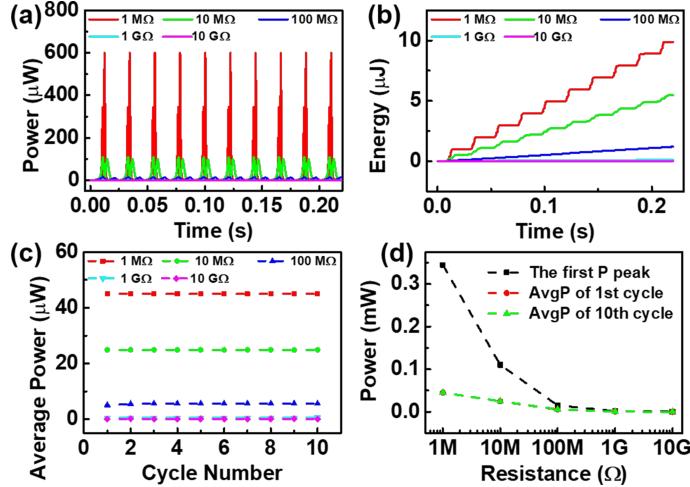
Fig.7. Output power and energy of the TENG calculated with different load resistances during the first 10 movement cycles, using the initial condition that the TENG starts working from the separated position. (a) Instantaneous output power ($P(t)$) of the TENG. (b) Output energy ($W(t)$) of the TENG. (c) Average output power per movement cycle ($AvgP$) of the TENG. (d) The first $P(t)$ peak value, and the $AvgP$ in the first and tenth movement cycles of the TENG with different load resistances.
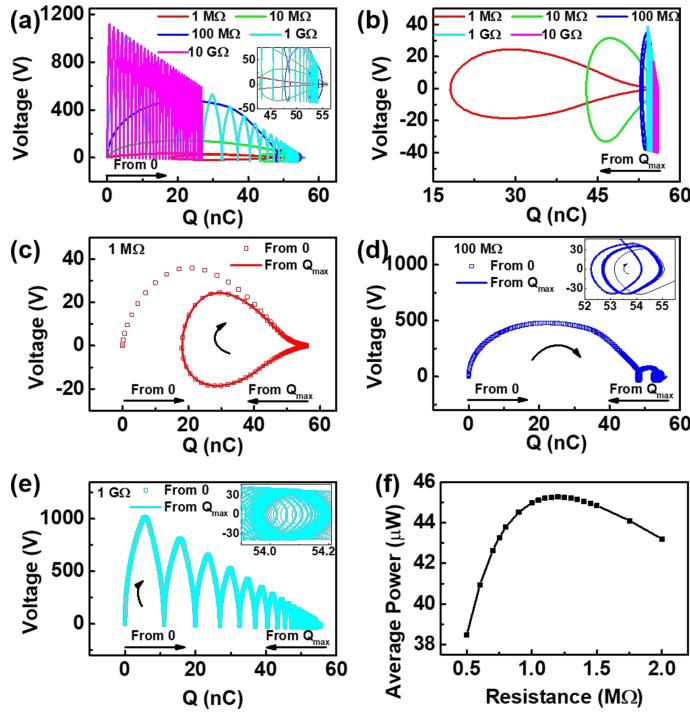
Fig.8. Comparisons in QV cycles calculated from the two different initial conditions. (a) QV cycle diagrams of the TENG calculated from the first initial condition with different load resistances. (b) QV cycle diagrams of the TENG calculated from the second initial condition with different load resistances. (c), (d), and (e) QV cycle diagrams of the TENG calculated from the first and second initial conditions with a load resistance of 1 MΩ, 100 MΩ, and 1 GΩ respectively. (f) The influence of the load resistance on the output average power per movement cycle of the TENG calculated from the second initial condition.
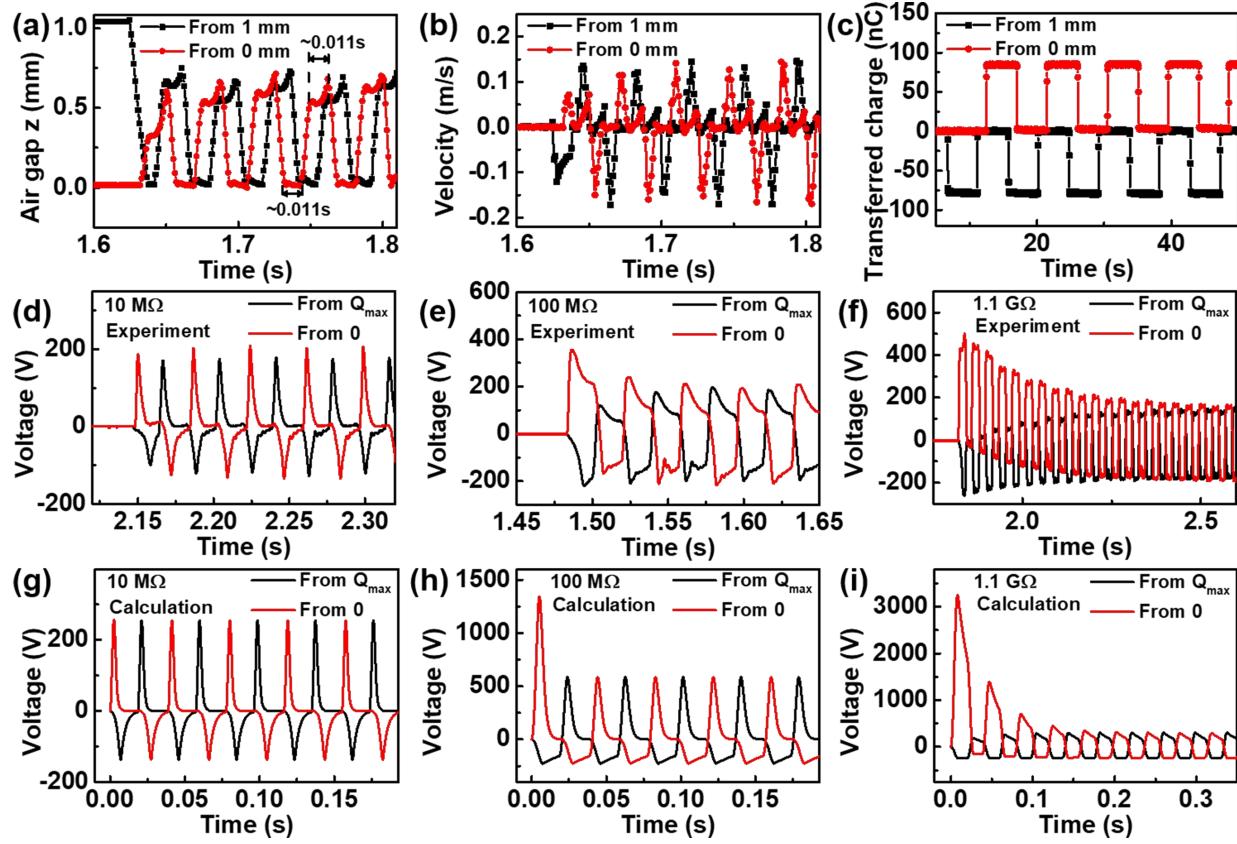
Fig.9. Experimental and calculated data for a PTFE electret film-based TENG that starts working from the contact and separated positions respectively. (a) The air gap data got from the linear motor system during the measurement of the TENG. (b) The movement velocity data got from the linear motor system during the measurement of the TENG. (c) The short-circuit transferred charge amount data of the TENG. (d), (e), and (f) Measured output voltage of the TENG with a load resistance of 10 MΩ, 100 MΩ, and 1.1 GΩ, respectively. (d), (e), and (f) Output voltage of the TENG calculated with a load resistance of 10 MΩ, 100 MΩ, and 1.1 GΩ, respectively.

Vitae

Hanlu Zhang received his M.S. degree (2016) of Materials Science from Zhengzhou University, under the supervision of Prof. Lin Dong, and he studied at the Beijing Institute of Nanoenergy and Nanosystems as a joint training master candidate during 2013~2015, co-supervised by Prof. Caofeng Pan. Now he is a CSC sponsored Ph.D. candidate directed by Prof. Jinbo Bai at CentraleSupélec of the University of Paris-Saclay. His current research interests are focused on preparations and characterizations of electrets and triboelectric nanogenerators.

Shan Feng received her B.S. and M.S. degree in Materials Science and Engineering from China University of Geosciences, under the supervision of Prof. Jin TAN. Now she is a CSC sponsored Ph.D. candidate directed by Prof. Jinbo Bai at CentraleSupélec of the University of Paris-Saclay. Her research mainly focuses on dielectric material synthesis and characterization, fabrication of triboelectric nanogenerators.

Delong He received his Ph.D. degree in materials science from Ecole Centrale Paris (France) in 2010. He conducted Post-doc research at CEA-Saclay in 2011 and then at CNRS MSSMat laboratory from 2012 to 2013. Since 2016, he is a permanent research engineer of CentraleSupélec (France). His research interests are multifunctional composite materials and energy.

Philippe Molinié was born in Suresnes, France, in 1965. He received the Engineering degree from the Ecole Supérieure d'Electricité (CentraleSupélec), Gif-sur-Yvette, France, in 1987, the Ph.D. degree from Université Pierre et Marie Curie, Paris, France, in 1992, and the Habilitation (H.D.R.) degree from Paris-Sud University, Orsay, France, in 2010. He is currently an Associate Professor with CentraleSupélec. His current research interests include electrostatics, dielectric materials characterization, and models of radiation-induced conductivity.
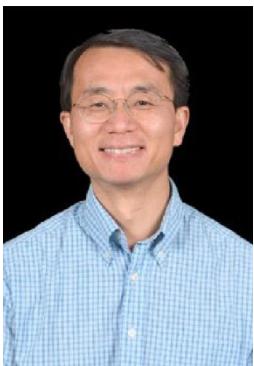
Jinbo Bai received his master's degree of Solid Mechanics from Xi'an Jiaotong University in 1985 and Ph.D. degree of Science of Materials from Ecole Centrale Paris in 1991. He was a lecturer of Mechanics of Materials in Northwestern Polytechnic University 1985-1987 and CNRS Researcher then Director of research in Lab. MSSMAT, UMR8579 of Ecole Centrale Paris since 1991. His research interest covers from nuclear materials Zr&Ti, hydrogen storage and embrittlement, composites materials, micromechanical modeling, finite element simulations, carbon nanomaterials' syntheses, characterizations and applications, structural and multi-functional nano/micro composites, hybrid fillers, heat management, energy storage and green energy in general.